LETTER • **OPEN ACCESS**

Purely rotational symmetry-protected topological crystalline insulator α-Bi_4Br_4

To cite this article: Chuang-Han Hsu *et al* 2019 *2D Mater.* **6** 031004

2D Materials

OPEN ACCESS

RECEIVED
7 January 2019

REVISED
19 March 2019

ACCEPTED FOR PUBLICATION
4 April 2019

PUBLISHED
22 May 2019

LETTER

Purely rotational symmetry-protected topological crystalline insulator α-Bi_4Br_4

Chuang-Han Hsu[1,2], Xiaoting Zhou[3], Qiong Ma[4], Nuh Gedik[4], Arun Bansil[5], Vitor M Pereira[1,2], Hsin Lin[6], Liang Fu[4], Su-Yang Xu[4] and Tay-Rong Chang[3,7]

[1] Department of Physics, National University of Singapore, Singapore 117542, Singapore
[2] Centre for Advanced 2D Materials and Graphene Research Centre, National University of Singapore, Singapore 117546, Singapore
[3] Department of Physics, National Cheng Kung University, Tainan, 701, Taiwan
[4] Department of Physics, Massachusetts Institute of Technology, Cambridge, MA 02139, United States of America
[5] Department of Physics, Northeastern University, Boston, MA 02115, United States of America
[6] Institute of Physics, Academia Sinica, Taipei 11529, Taiwan
[7] Center for quantum frontiers of research & technology (QFort), Tainan, 701, Taiwan

E-mail: liangfu@mit.edu, suyangxu@mit.edu and u32trc00@phys.ncku.edu.tw

Keywords: topological crystalline insulators, higher-order topological insulators, α-Bi_4Br_4, spin accumulation, first-principles calculations

Supplementary material for this article is available online

Abstract

Rotational-symmetry-protected topological crystalline insulators (TCIs) are expected to host unique boundary modes, in that the surface normal to the rotational axis can feature surface states with 'unpinned' Dirac points, which are not constrained to lie on high symmetry points or lines, but can lie at any general k point in the Brillouin zone. Also, as a higher order bulk boundary correspondence is involved here, a three-dimensional (3D) TCI can support one-dimensional (1D) helical edge states. Using first-principles band structure calculations, we identify the van der Waals material α-Bi_4Br_4 as a purely rotation symmetry protected TCI. We show that the (0 1 0) surface of Bi_4Br_4 exhibits a pair of unpinned topological Dirac fermions which are related to the presence of a two-fold rotation axis. These unpinned Dirac fermions possess an exotic spin texture which will be highly favorable for spin transport, and a band structure that consists of van Hove singularities due to a Lifshitz transition. We also identify 1D topological hinge states along the edges of an α-Bi_4Br_4 rod. We comment on how the predicted topological features in α-Bi_4Br_4 could be accessed experimentally.

1. Introduction

Topological crystalline insulators (TCIs) are insulators in which the nontrivial band topology is protected by crystalline symmetries [1–4]. Although the availability of a large number of crystalline space groups suggests the existence of a rich variety of TCI states, to date, only mirror symmetry-protected TCIs have been experimentally identified [4–19]. Recently, a new class of TCIs, where the protection is through the presence of N-fold rotational symmetries, has been proposed [20]. The rotation symmetry protected TCIs are distinct from the common topological insulators (TIs). For example, the surface normal to the rotational axis in these TCIs hosts N Dirac cones where the Dirac points can appear at any general k point in the surface Brillouin zone (BZ) and are not restricted to lie on high symmetry points or lines in the BZ. Moreover, such a 3D TCI can support 1D topological edge states due to the higher order bulk-boundary correspondence involved in this case [21–27]. Additionally, in a rod with N-fold rotational symmetry that is finite sized along the two directions perpendicular to the rotational axis, the hinges of the rod host N helical 1D edge states.

Experimental realization of purely rotational symmetry-protected TCIs has, however, remained elusive in real materials. One challenge is that the rotational-symmetry related topological invariants are difficult to compute in first-principles calculations as they are defined in terms of Wannier center flows [28]. Recent progress in this connection relates crystalline symmetry-protected topological invariants with symmetry eigenvalues of the electronic states [29–36]. In particular, Song *et al* [32] and Khalaf *et al* [33], found that when a certain additional symmetry Y is present, the topological invariants of TCIs protected

by symmetry X can be inferred from the Y-symmetry eigenvalues of energy bands. This proposal of symmetry indicators has facilitated first-principles studies of new TCIs [37–41].

Another challenge involves how to isolate the nontrivial topology protected by the rotational symmetry from that protected by the mirror symmetry. We illustrate this point by taking the example of a tetragonal crystal lattice with point group D_{4h} (space group $P4/mmm$). The nontrivial topology protected by the out-of-the-plane four-fold rotational symmetry $4_{[0\,0\,1]}$ would lead here to four Dirac fermions on the $(0\,0\,1)$ surface, see figure 1(a). (The conventional basis is used for $[h\,k\,l]$ and $(h\,k\,l)$, see supplementary materials (stacks.iop.org/TDM/6/031004/mmedia)). However, the band topology that gives rise to the nontrivial $4_{[0\,0\,1]}$ index is likely to harbor the mirror-symmetry-protected nontrivial topology in the mirror planes ($M_{[1\,0\,0]}$, $M_{[0\,1\,0]}$, $M_{[1\,1\,0]}$ and $M_{[1-1\,0]}$). Consequently, the four Dirac fermions must be located along the $[1\,0\,0]$, $[0\,1\,0]$, $[1\,1\,0]$ or $[1\bar{1}0]$ high-symmetry directions (figure 1(a)).

We surmise that a particular class of monoclinic lattices with the point group C_{2h} are ideally suited to searching for purely rotational symmetry-protected TCIs. Our reasoning is as follows. As shown in figure 1(b), a C_{2h} lattice supports three symmetry operations, a two-fold rotational axis $2_{[0\,1\,0]}$, a mirror plane $M_{[0\,1\,0]}$, and the space inversion symmetry $\mathcal{I}$. Interestingly, the $(0\,1\,0)$ surface only preserves the two-fold rotational symmetry $2_{[0\,1\,0]}$ but breaks $M_{[0\,1\,0]}$. On the other hand, the presence of the inversion symmetry $\mathcal{I}$ in the bulk still allows for the application of the symmetry indicator scheme. These considerations suggest that C_{2h} crystals are ideal for searching for purely rotational symmetry-protected TCIs and that two unpinned Dirac fermions can appear at general k points on the $(0\,1\,0)$ surface due to the nontrivial topology protected by $2_{[0\,1\,0]}$.

Guided by the preceding analysis, we have carefully searched for materials with a monoclinic C_{2h} lattice. From this, we identified the van der Waals material α-Bi_4Br_4 as a TCI which is purely protected by rotational symmetry. Figure 1(c) illustrates the experimentally determined lattice structure of α-Bi_4Br_4 with point group C_{2h} (space group $C2/m$ (#12)) [42, 43]. Consistent with figure 1(b), the two-fold rotational axis in α-Bi_4Br_4 lies along the $[0\,1\,0]$ direction (figure 1(c)). Notably, recent experiments [44–46] have identified a topological insulator state in the sister compound β-Bi_4I_4, and a weak TI phase has been predicted in β-Bi_4Br_4 [47], see supplementary materials. On the other hand, the electronic and topological properties of α-Bi_4Br_4 remain unexplored, although its monolayer has been proposed to host a 2D quantum spin Hall insulator state [48].

2. Method

The first-principles calculations were based on the generalized gradient approximation (GGA) [57] using the full-potential projector augmented wave method [58, 59] as implemented in the VASP package [60, 61]. The experimental crystal structure of α-Bi_4Br_4 was used [42]. The electronic structure of bulk α-Bi_4Br_4 was calculated using a $15 \times 15 \times 5$ Monkhorst–Pack k-mesh over the Brillouin zone (BZ) with the spin–orbit coupling (SOC) included self-consistently. We used Bi and Br p orbitals to construct Wannier functions, without performing the procedure for maximizing localization [62]. The surface spectral weight was computed via a semi-infinite Green's function method [63] using our effective Wannier tight-binding Hamiltonian. We also constructed a C_2-preserved 1D tube with a size close to $4 \times 1 \times 4$ supercell from our Wannier Hamiltonian to examine the 1D hinge states, see figures 2(e) or S3 of the supplementary material for details of the crystal structure.

3. Crystal structure and band topology

Band structure calculations were carried out using the VASP package [49] and the experimental crystal structure of α-Bi_4Br_4 [42]. The Wannier [50] based tight-binding model was used for investigating surface states. The bulk band structure with spin–orbit coupling (SOC) (figure 1(d)) shows a band gap around 0.4 eV. The bands at low energies are dominated by four bands, two conduction bands (CBs) and two valence bands (VBs), all of which mainly involve the Bi $6p$-orbitals. By examining the evolution of the band structure as a function of SOC strength, we identified an even number of band inversions between bands of opposite parity eigenvalues at the L point. The first band inversion between VBs and CBs can be seen from figures 1(f)–(g), which show how a trivial insulator evolves into a strong TI (STI). Subsequently (figure 1(h)), the CBs and VBs experience internal band inversions without closing the band gap and maintain the STI phase. In the final stage, another band inversion between the VBs and CBs takes place as seen in figures 1(h)–(i). The presence of an even number of band inversions rules out the possibility that the α-Bi_4Br_4 hosts a time-reversal symmetry-protected Z_2 STI state. Interestingly, a rotation symmetry-protected TCI state can be derived from bands hosting two strong TI representations [20] where two band inversions will be needed. In other words, the two band inversions between VBs and CBs in α-Bi_4Br_4 can give rise to a rotation symmetry-protected TCI state.

We now turn to discuss the symmetry-based indicators (SIs). As shown in [32, 33], crystals in space group #12 are characterized by four symmetry indicators, three $\mathbb{Z}_2$ indices and one $\mathbb{Z}_4$ ($\mathbb{Z}_{2,2,2,4}$) index. By enumerating the symmetry eigenvalues of the electron states at high symmetry points, we obtain $\mathbb{Z}_{2,2,2,4} = \{0, 0, 0, 2\}$ in α-Bi_4Br_4. Table 1 shows the topological states corresponding to $\mathbb{Z}_{2,2,2,4} = \{0, 0, 0, 2\}$, following [32], see the caption of table 1 for the definition of various invariants. Importantly, the symmetry indicators

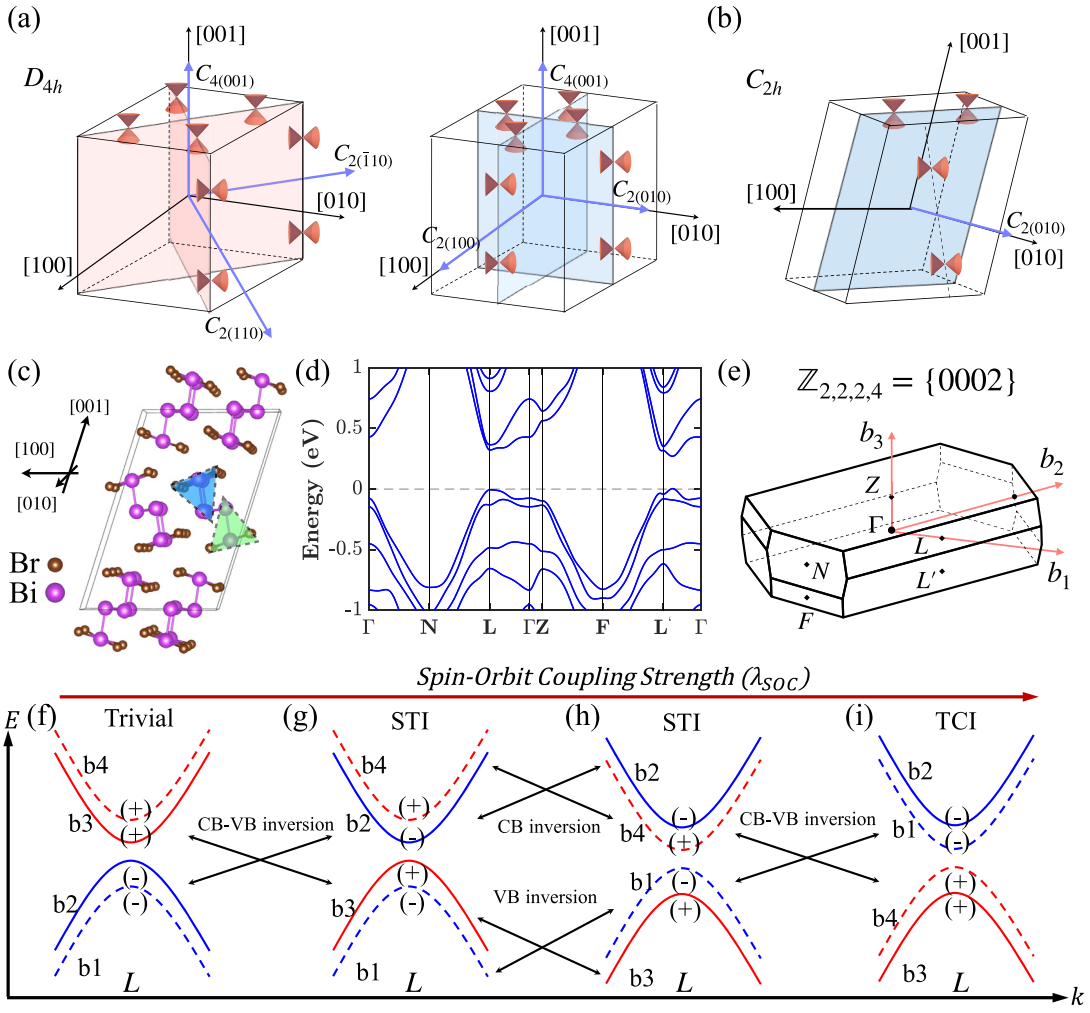

Figure 1. (a) Schematic illustrations of TCI surface states on different surfaces for a tetragonal D_{4h} lattice. In a D_{4h} lattice, we expect the nontrivial topology protected by the out-of-the-plane four-fold rotational symmetry $4_{[0\,0\,1]}$ to yield four Dirac fermions on the (0 0 1) surface. However, due to the presence of the nontrivial mirror planes ($M_{[1\,0\,0]}$, $M_{[0\,1\,0]}$, $M_{[1\,1\,0]}$ and $M_{[1\,\bar{1}\,0]}$), the four Dirac fermions must be located along the [1 0 0],[0 1 0],[1 1 0] or [1 $\bar{1}$ 0] high-symmetry direction. (b) A C_{2h} lattice consists of three symmetry operations, a two-fold rotational axis $2_{[0\,1\,0]}$, a mirror plane $M_{[0\,1\,0]}$, and space-inversion symmetry $\mathcal{I}$. The (0 1 0) surface, however, only hosts the two-fold rotational symmetry $2_{[0\,1\,0]}$. Therefore, C_{2h} crystals are ideal for searching for purely rotational symmetry-protected TCIs and the two associated unpinned Dirac fermions that can appear at general k points on the (0 1 0) surface protected by $2_{[0\,1\,0]}$. (c) Crystal structure of α-Bi_4Br_4. (d) Bulk band structure with SOC. (e) Bulk BZ of α-Bi_4Br_4 with the high-symmetry points marked. Crystals in space group #12, which include α-Bi_4Br_4, are characterized by four symmetry indicators, three $\mathbb{Z}_2$ and one $\mathbb{Z}_4$ ($\mathbb{Z}_{2,2,2,4}$) [32, 33]. For α-Bi_4Br_4, our calculations show that $\mathbb{Z}_{2,2,2,4} = \{0002\}$. (f)–(i) Schematic illustration of the evolution of the low-energy band structure as a function of the strength of the SOC near the L point. The parity eigenvalues of the electron states at L are labeled. A topologically trivial state is obtained in (f), strong topological insulator states (STIs) are obtained in (g) and (h), and a topological crystalline insulator (TCI) phase is obtained in (i).

($\mathbb{Z}_{2,2,2,4} = \{0, 0, 0, 2\}$) point to two possible topological states, one being a purely rotational symmetry-protected TCI with $n_{2_{[0\,1\,0]}} = 1$, and the other a purely mirror symmetry-protected TCI with $n_{\mathcal{M}_{[0\,1\,0]}} = 2$. Note that the $\mathcal{I}$-protected topology is referred to as a higher-order topological insulator (HOTI) [25], and is not considered here. In order to uniquely determine the topological state of α-Bi_4Br_4, we have further calculated the mirror Chern number $n_{\mathcal{M}_{[0\,1\,0]}}$, and found $n_{\mathcal{M}_{[0\,1\,0]}} = 0$ for α-Bi_4Br_4. These results thus reveal that α-Bi_4Br_4 is a purely rotational symmetry-protected TCI with $n_{2_{[0\,1\,0]}} = 1$.

We emphasize that according to [32], crystals in space group #12 cannot host a weak TI and a rotational symmetry-protected TCI phase at the same

Table 1. The two possible topological states for the symmetry indicator $\mathbb{Z}_{2,2,2,4} = \{0, 0, 0, 2\}$ [32], where $(\nu_0; \nu_1\nu_2\nu_3)$ are the $\mathbb{Z}_2$ invariants for a 3D $\mathbb{Z}_2$ TIs, and are all seen to be zero, indicating that the state is neither a strong nor a weak TI. $n_{2_{[0\,1\,0]}}$ is the topological invariant for the two-fold rotational symmetry $2_{[0\,1\,0]}$; it is also a $\mathbb{Z}_2$ invariant. $n_{2_{[0\,1\,0]}} = 1$ corresponds to a rotational symmetry-protected TCI, which features two unpinned Dirac surface states on the (0 1 0) surface. $n_{\mathcal{M}_{[0\,1\,0]}}$ is the topological invariant for the mirror plane $\mathcal{M}_{[0\,1\,0]}$ (the mirror Chern number), and is a $\mathbb{Z}_N$ invariant. $n_{\mathcal{M}_{[0\,1\,0]}} = N$ corresponds to a mirror symmetry-protected TCI, which features N Dirac surface states, see supplementary materials for a discussion of the symmetry indicators and the related topological invariants.

$(\nu_0; \nu_1\nu_2\nu_3)$	$n_{2_{[0\,1\,0]}}$	$n_{\mathcal{M}_{[0\,1\,0]}}$
(0;000)	1	0
(0;000)	0	2

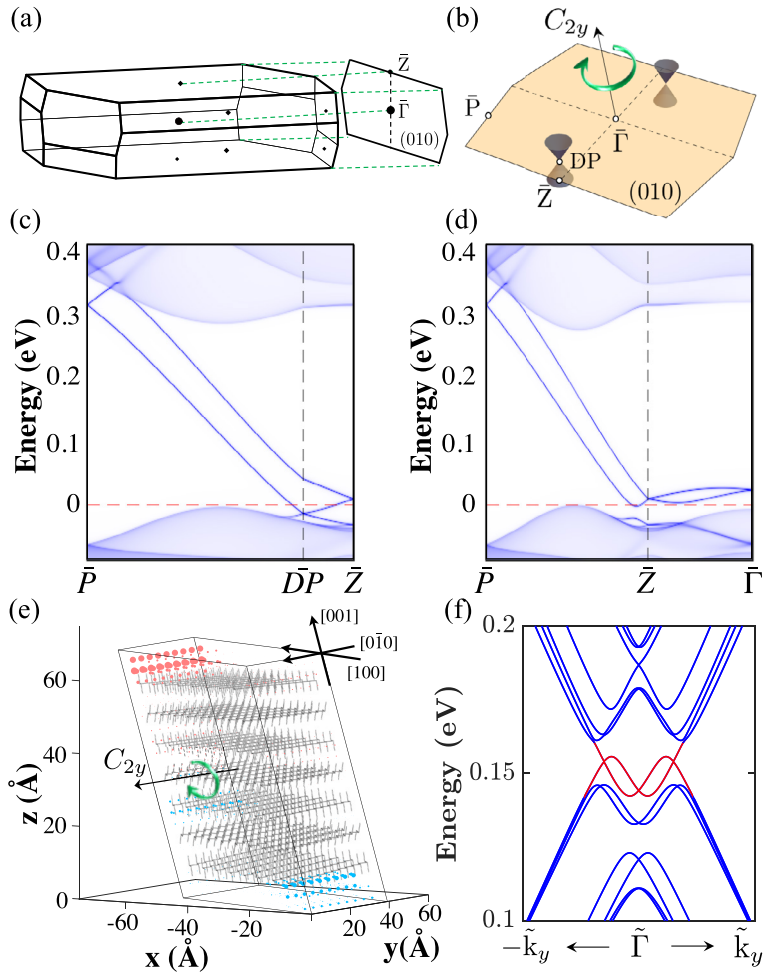

Figure 2. (a) Bulk BZ and the (0 1 0) surface BZ. (b) Schematic illustration of the unpinned topological Dirac cones protected by the two-fold rotational symmetry $2_{[0\,1\,0]}$ on the (0 1 0) surface. (c) and (d) Calculated (0 1 0) surface states along $\bar{P}-\bar{DP}-\bar{Z}$ and $\bar{P}-\bar{Z}-\bar{\Gamma}$. (f) Band structure of a 1D 4×1×4 α-Bi_4Br_4 nanorod that is finite-sized along $[\bar{1}\,1\,0]$ and [0 0 1] but periodic along [0 1 0]. (e) Real-space distribution of the nontrivial edge state indicated by the red curves shown in (f). The crystal structure of a 1D $4\times1\times4$ supercell is shown by gray rods corresponding to the bonds between Bi, where the Br atoms are neglected to help visualization.

time. Therefore, α-Bi_4Br_4 cannot be a weak TI, and the predicted weak TI β-Bi_4Br_4 [47] cannot be a rotational symmetry-protected TCI.

4. Surface states

In order to confirm the topological nature of α-Bi_4Br_4, we investigated its novel topological boundary modes. We first focus on uncovering the unpinned Dirac surface states on the (0 1 0) surface protected by the two-fold rotational symmetry $2_{[0\,1\,0]}$. By calculating the band structure throughout the (0 1 0) surface BZ, we identified two Dirac cones. Their Dirac points (DPs) are located at $\pm(0.0434\,\frac{2\pi}{a}, 0.3550\,\frac{2\pi}{c})$. These are seen to be general k points, as expected, which are only related by the two-fold rotational symmetry $2_{[0\,1\,0]}$. The calculated surface states along a k path passing through the DP ($\bar{P}-\bar{DP}-\bar{Z}$, figure 2(c)) directly shows the topological Dirac surface states. On the other hand, along the path $\bar{P}-\bar{Z}-\bar{\Gamma}$ that does not go through the DP, the surface states are gapped (figure 2(d)).

We next discuss the 1D topological hinge states protected by $2_{[0\,1\,0]}$. For this purpose, we calculated the band structure of a 1D α-Bi_4Br_4 rod that is finite-sized along $[\bar{1}\,1\,0]$ and [0 0 1] but periodic along [0 1 0] (see the supplementary material for details of the crystal structure). Figure 2(f) shows the existence of 1D helical edge states inside the bulk band gap. We also explored the real-space distribution of the electron wave functions of the 1D helical edge states. As shown in figure 2(e), these states are localized on the edges shared by adjacent side surfaces, confirming that they are indeed topological hinge states. Experimentally, the unpinned Dirac surface states could be directly imaged via photoemission spectroscopy, whereas the helical hinge states could be probed via scanning-tunneling spectroscopy. Although it was challenging, the band structure of the hinge states (figure 2(f)) indicates that a quantized longitudinal charge conductivity (σ_{yy}) could be measured on the 1D structure proposed here.

We further highlight the novel electronic properties enabled by the unpinned topological Dirac fermions on the (0 1 0) surface. We first discuss the existence of van Hove singularities (VHSs) on the (0 1 0) surface. At an energy close to the Dirac point ($E = 2.9$ meV), the surface state exhibits two separated electron-like

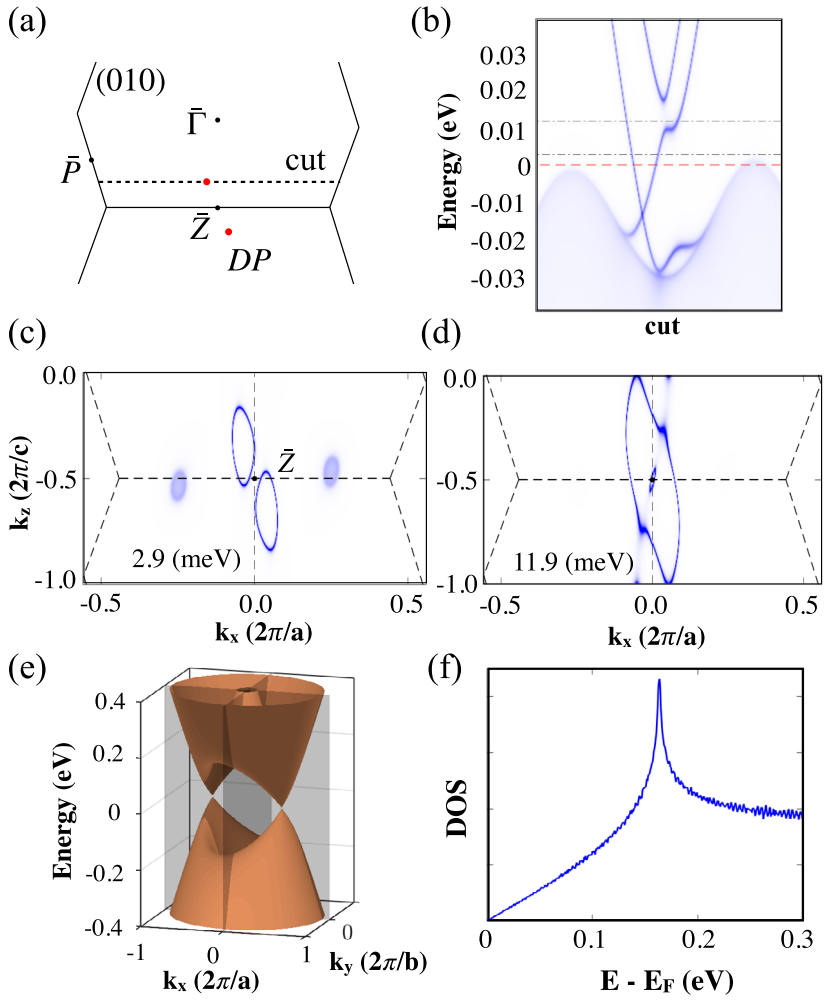

Figure 3. (a) The (0 1 0) surface BZ. Red points denote the center of the unpinned Dirac cones. (b) The surface state band structure calculated along the path marked by the black dotted line in (a). (c) and (d) Constant energy contours at the binding energies of 2.9 meV and 11.9 meV (indicated in panel (b) by the dotted lines). A Lifshitz transition is observed as two separate contours (panel (c)) merge and become two concentric contours (panel (d)). (e) and (f) Electronic structure generated by the $k \cdot p$ model that describes a pair of unpinned Dirac cones on the (0 1 0) surface of α-Bi_4Br_4. (f) Calculated DOS as a function of energy based on our $k \cdot p$ model. A sharp DOS peak is seen at the energy corresponding to the Lifshitz transition, and the associated VHS.

contours (figure 3(c)). As one goes to higher energies above the Dirac point, the contours expand and eventually merge. At $E = 11.9$ meV, two concentric contours emerge (figure 3(d)). Such a Lifshitz transition signals the presence of a saddle point in the surface electronic band structure, and an associated VHS with diverging density of states (DOS). In order to gain insight into the nature of Dirac surface states and their relationship to the VHS, we have constructed an effective $k \cdot p$ model. Note that the (0 1 0) surface supports two symmetries, the two fold rotation $2_{[0\,1\,0]}$ and time-reversal $\mathcal{T}$. Based on our first-principles calculations, we have chosen the following symmetry adapted bases for the $k \cdot p$ model. $|\Psi_{\mathbf{k}}\rangle = (\psi_{+\uparrow}, \psi_{+\downarrow}, \psi_{-\uparrow}, \psi_{-\downarrow})^T$ as,

$$|\psi_{\pm,s}\rangle = \sum_{\alpha=x,z} \lambda_\alpha s(|p^A_\alpha, s\rangle \pm |p^B_\alpha, s\rangle) + \lambda_y s(|p^A_y, s\rangle \mp |p^B_y, s\rangle), \quad (1)$$

where $\pm$ is the eigenvalue of $2_{[0\,1\,0]} \times \mathcal{T}$, s $(=\uparrow\downarrow)$ is the spin index, and λ_i is the orbital weight for the p_i orbital. The A and B sub-lattices are indicated by the blue and green triangles in figure 1(c) (the (0 1 0) surface here is spanned by the x-z plane). The simplest 4×4 dimensional model including all the allowed constant terms δ_{ij} takes the form,

$$H(\mathbf{k}) = v_R\tau_0(k_x\sigma_1 - k_z\sigma_3) + \delta_{30}\tau_3\sigma_0 + \delta_{21}\tau_2\sigma_1 + \delta_{23}\tau_2\sigma_3, \quad (2)$$

where the Pauli matrices σ_i and τ_i denote the spin and sub-lattice degrees of freedom, respectively. As shown in figures 3(e) and (f), the Lifshitz transition is reproduced by our $k \cdot p$ model. The DOS as a function of energy based on this $k \cdot p$ model, shows the expected divergent behavior at the energy position of the VHS (figure 3(f)). The VHS and the related diverging DOS are favorable conditions for the appearance of correlated quantum phenomena [51–53].

We now discuss the spin texture of the unpinned Dirac fermions and their implications for spin transport. At energies close to the surface Dirac points (see, for example, figure 3(c)), the spin texture is quite similar to that of existing topological insulators in

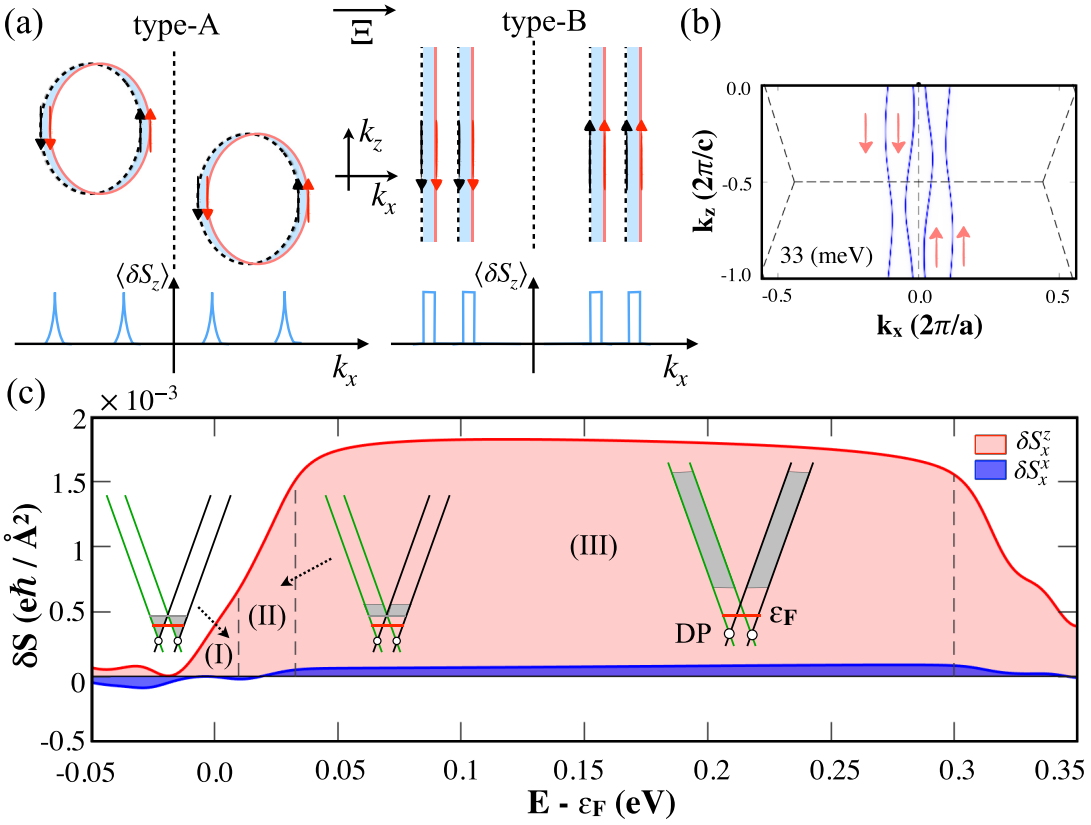

Figure 4. (a) The schematic picture illustrates the non-equilibrium spin density (δS) driven by the external electric field (Ξ) for the type-A (left) Fermi surface (figure 3(c)). Results for the type-B case (right) are shown in (b) for $\mu = 33$ meV on the α-Bi_4Br_4 (0 1 0) surface. Black-dashed lines are the Fermi contours at equilibrium, and the red lines are the corresponding Fermi contours under the field Ξ. The blue shaded areas indicate the induced δS due to the Fermi surface shift. By examining the spin textures of the surfaces states in (b), we found that the Fermi contours on the right hand side of the $k_x = 0$ line host up spin-z states, while the two on the left hand side of the $k_x = 0$ line host down spin-z states, as indicated by the arrows. (c) Calculated δS on the α-Bi_4Br_4 (0 1 0) surfaces. δS in the areas (I) and (III) is given predominantly by the type-A and type-B cases discussed in (a), respectively. The energy windows for the regions (I) to (III) are indicated by the gray areas on the schematic E-k diagrams, while the Fermi energy ε_F is indicated by the red lines in schematic Dirac cones.

that the spin polarization winds tangentially around the closed constant energy contours. On the other hand, as we move to energies further away from the Dirac point (e.g. $E = 33$ meV in figure 4(b)), the constant energy contours evolve into separated lines that traverse the whole surface BZ. Interestingly, in this regime, the spin texture of two left movers are dominantly up spin-z whereas the two right movers are down spin-z (the spin orientation is indicated by the red arrow in figure 4(b)), realizing a 3D quantum spin Hall effect [9]. Importantly, in α-Bi_4Br_4, this spin texture is realized in a large energy window (0–300 meV) driven by the large bulk energy band gap. This unique spin texture could lead to a large spin transport effect. In this connection, we have calculated the current-induced spin accumulation (δS) due to the Rashba–Edelstein effect [54], i.e. passing an electrical current tilts the Fermi surface out of its equilibrium distribution, yielding a net spin polarization. We thus expect a sizeable accumulation of the spin polarization along z (S^z) when passing an electrical current along the x direction. Note that the spin accumulation can be calculated within the linear response theory [55] as follows.

$$\delta \mathbf{S} = \frac{e\hbar}{\Gamma V} \sum_n \delta(\varepsilon_\mathbf{F} - \varepsilon_n) \langle n|\mathbf{S}|n\rangle \langle n|\mathbf{v} \cdot \Xi|n\rangle, \quad (3)$$

where e, $\hbar$, V and Γ are the unit charge, the Planck constant, volume of the unit cell, and broadening due to impurities, respectively, $\varepsilon_\mathbf{F}$ is the Fermi energy, ε_n is the energy eigenvalue of the state $|n\rangle$, and $\mathbf{S}$, $\mathbf{v} = \frac{\partial H(\mathbf{k})}{\hbar \partial \mathbf{k}}$ and Ξ denote the spin, velocity and the external electric field. The calculated results are shown in figure 4(c), where δS_β^α gives the spin polarization along the α direction by following an external current along the β direction. The largest response is indeed δS_x^z. In regime (I), the surface states (SSs) and the spin texture resemble two copies of TI centered at generic momenta (referred to as type-A behavior, figure 4(a)). δS_x^z increases with increasing energy since the two Fermi surface contours enlarge. For regime (III), the four parallel Fermi contours with high s_z polarization lead to the largest δS_x^z, which is almost constant in this regime due to its quasi-1D characteristic (referred to as type-B behavior, Fig 4(a)). Regime II is a crossover region that connects regimes I and III. We expect that this unique spin accumulation can be directly probed by Kerr rotation microscopy [56].

5. Conclusion

In conclusion, our analysis based on first-principles computations shows that α-Bi_4Br_4 is a candidate material for the newly proposed C_2-protected TCIs. Existence of this unique TCI phase is confirmed by the presence of unpinned Dirac surface states on the (0 1 0) surface, and of 1D topological hinge states on a C_2 preserving α-Bi_4Br_4 nanorod. Moreover, we have delineated the evolution of (0 1 0) surface states as a function of energy above the Dirac points to show that α-Bi_4Br_4 hosts a 3D quantum-spin-Hall-effect, and can thus be expected to support large spin transport.

Acknowledgments

T-RC and XZ were supported by the Young Scholar Fellowship Program by Ministry of Science and Technology (MOST) in Taiwan, under MOST Grant for the Columbus Program MOST108-2636-M-006-002, National Cheng Kung University, Taiwan, and National Center for Theoretical Sciences (NCTS), Taiwan. This work is supported partially by the MOST, Taiwan, Grants No. MOST 107-2627-E-006-001. The work at Northeastern University was supported by the US Department of Energy (DOE), Office of Science, Basic Energy Sciences Grant No. DE-FG02-07ER46352, and benefited from Northeastern University's Advanced Scientific Computation Center (ASCC) and the NERSC supercomputing center through DOE grant number DE-AC02-05CH11231. LF was supported by DOE Office of Basic Energy Sciences, Division of Materials Sciences and Engineering under Award DE-SC0018945. NG and SYX acknowledge support by the STC Center for Integrated Quantum Materials, NSF Grant No. DMR-1231319.

Note added. After we had submitted our manuscript, [38] came to our attention, which also proposes α-Bi_4Br_4 as a rotation-symmetry protected TCI.

ORCID iDs

Chuang-Han Hsu https://orcid.org/0000-0002-2394-8537
Hsin Lin https://orcid.org/0000-0002-4688-2315
Tay-Rong Chang https://orcid.org/0000-0003-1222-2527

References

[1] Hasan M Z and Kane C L 2010 Colloquium: Topological insulators *Rev. Mod. Phys.* **82** 3045–67
[2] Qi X-L and Zhang S-C 2011 Topological insulators and superconductors *Rev. Mod. Phys.* **83** 1057–110
[3] Bansil A, Lin H and Das T 2016 Colloquium: Topological band theory *Rev. Mod. Phys.* **88** 021004
[4] Fu L 2011 Topological crystalline insulators *Phys. Rev. Lett.* **106** 106802
[5] Teo J C, Fu L and Kane C 2008 Surface states and topological invariants in three-dimensional topological insulators: application to $Bi_{1-x}Sb_x$ *Phys. Rev.* B **78** 045426
[6] Hsieh T H, Lin H, Liu J, Duan W, Bansil A and Fu L 2012 Topological crystalline insulators in the SnTe material class *Nat. Commun.* **3** 982
[7] Weng H, Zhao J, Wang Z, Fang Z and Dai X 2014 Topological crystalline kondo insulator in mixed valence ytterbium borides *Phys. Rev. Lett.* **112** 016403
[8] Wieder B J, Bradlyn B, Wang Z, Cano J, Kim Y, Kim H-S D, Rappe A, Kane C and Bernevig B A 2018 Wallpaper fermions and the nonsymmorphic Dirac insulator *Science* **361** 246–51
[9] Wang Z, Alexandradinata A, Cava R J and Bernevig B A 2016 Hourglass fermions *Nature* **532** 189–94
[10] Tanaka Y, Ren Z, Sato T, Nakayama K, Souma S, Takahashi T, Segawa K and Ando Y 2012 Experimental realization of a topological crystalline insulator in SnTe *Nat. Phys.* **8** 800–3
[11] Dziawa P *et al* 2012 Topological crystalline insulator states in $Pb_{1-x}Sn_xTe$ *Nat. Mater.* **11** 1023–7
[12] Xu S-Y 2012 Observation of a topological crystalline insulator phase and topological phase transition in $Pb_{1-x}Sn_xTe$ *Nat. Commun.* **3** 1192
[13] Okada Y *et al* 2013 Observation of Dirac node formation and mass acquisition in a topological crystalline insulator *Science* **341** 1496–9
[14] Zeljkovic I *et al* 2014 Mapping the unconventional orbital texture in topological crystalline insulators *Nat. Phys.* **10** 572–7
[15] Liang T, Gibson Q, Xiong J, Hirschberger M, Koduvayur S, Cava R and Ong N 2013 Evidence for massive bulk Dirac fermions in $Pb_{1-x}Sn_xSe$ from Nernst and thermopower experiments *Nat. Commun.* **4** 2696
[16] Li X and Niu Q 2017 Topological phase transitions in thin films by tuning multivalley boundary-state couplings *Phys. Rev.* B **95** 241411
[17] Chang K *et al* 2016 Discovery of robust in-plane ferroelectricity in atomic-thick SnTe *Science* **353** 274–8
[18] Sessi P *et al* 2016 Robust spin-polarized midgap states at step edges of topological crystalline insulators *Science* **354** 1269–73
[19] Liang T, Kushwaha S, Kim J, Gibson Q, Lin J, Kioussis N, Cava R J and Ong N P 2017 A pressure-induced topological phase with large Berry curvature in $Pb_{1-x}Sn_xTe$ *Sci. Adv.* **3** e1602510
[20] Fang C and Fu L 2017 Rotation anomaly and topological crystalline insulators (arXiv:1709.01929)
[21] Song Z, Fang Z and Fang C 2017 $(d-2)$-dimensional edge states of rotation symmetry protected topological states *Phys. Rev. Lett.* **119** 246402
[22] Schindler F, Cook A M, Vergniory M G, Wang Z, Parkin S S, Bernevig B A and Neupert T 2018 Higher-order topological insulators *Sci. Adv.* **4** eaat0346
[23] Khalaf E 2018 Higher-order topological insulators and superconductors protected by inversion symmetry *Phys. Rev.* B **97** 205136
[24] Matsugatani A and Watanabe H 2018 Connecting higher-order topological insulators to lower-dimensional topological insulators *Phys. Rev.* B **98** 205129
[25] Schindler F *et al* 2018 Higher-order topology in bismuth *Nat. Phys.* **14** 1–12
[26] Wang Z, Wieder B J, Li J, Yan B and Bernevig B A 2018 Higher-order topology, monopole nodal lines and the origin of large Fermi arcs in transition metal dichalcogenides XTe_2 (X = Mo, W) (arXiv:1806.11116)
[27] Yue C, Xu Y, Song Z, Lu Y-M, Weng H, Fang C and Dai X 2019 Symmetry enforced chiral hinge states and surface quantum anomalous Hall effect in magnetic axion insulator $Bi_{2-x}Sm_xSe_3$ *Nat. Phys.* (https://doi.org/10.1038/s41567-019-0457-0)
[28] Taherinejad M, Garrity K F and Vanderbilt D 2014 Wannier center sheets in topological insulators *Phys. Rev.* B **89** 115102

[29] Bradlyn B, Elcoro L, Cano J, Vergniory M, Wang Z, Felser C, Aroyo M and Bernevig B A 2017 Topological quantum chemistry *Nature* **547** 298
[30] Kruthoff J, de Boer J, van Wezel J, Kane C L and Slager R-J 2017 Topological classification of crystalline insulators through band structure combinatorics *Phys. Rev.* X **7** 041069
[31] Po H C, Vishwanath A and Watanabe H 2017 Symmetry-based indicators of band topology in the 230 space groups *Nat. Commun.* **8** 50
[32] Song Z, Zhang T, Fang Z and Fang C 2018 Mapping symmetry data to topological invariants in nonmagnetic materials *Nat. Commun.* **9** 3530
[33] Khalaf E, Po H C, Vishwanath A and Watanabe H 2018 Symmetry indicators and anomalous surface states of topological crystalline insulators *Phys. Rev.* X **8** 031070
[34] Song Z, Zhang T and Fang C 2018 Diagnosis for topological semimetals in the absence of spin–orbital coupling *Phys. Rev.* X **8** 031069
[35] Bradlyn B, Elcoro L, Vergniory M, Cano J, Wang Z, Felser C, Aroyo M and Bernevig B A 2018 Band connectivity for topological quantum chemistry: band structures as a graph theory problem *Phys. Rev.* B **97** 035138
[36] Cano J, Bradlyn B, Wang Z, Elcoro L, Vergniory M, Felser C, Aroyo M and Bernevig B A 2018 Building blocks of topological quantum chemistry: elementary band representations *Phys. Rev.* B **97** 035139
[37] Zhou X *et al* 2018 Topological crystalline insulator states in the Ca_2As family *Phys. Rev.* B **98** 241104
[38] Tang F, Po H C, Vishwanath A and Wan X 2019 Efficient topological materials discovery using symmetry indicators *Nat. Phys.* **15** 470–6
[39] Tang F, Po H C, Vishwanath A and Wan X 2019 Topological materials discovery By Large-order symmetry indicators *Sci. Adv.* **5** eaau8725
[40] Zhang T, Jiang Y, Song Z, Huang H, He Y, Fang Z, Weng H and Fang C 2019 Catalogue of topological electronic materials *Nature* **566** 475–9
[41] Vergniory M, Elcoro L, Felser C, Bernevig B and Wang Z 2019 The (high quality) topological materials in the world *Nature* **566** 480–5
[42] von Benda H, Simon A and Bauhofer W 1978 Zur Kenntnis von BiBr und $BiBr_{1.167}$ *Z. Anorg. Allg. Chem.* **438** 53–67
[43] Filatova T, Gurin P, Kloo L, Kulbachinskii V, Kuznetsov A, Kytin V, Lindsjo M and Popovkin B 2007 Electronic structure, galvanomagnetic and magnetic properties of the bismuth subhalides Bi_4I_4 and Bi_4Br_4 *J. Solid State Chem.* **180** 1103–9
[44] Autès G *et al* 2015 A novel quasi-one-dimensional topological insulator in bismuth iodide β-Bi_4I_4 *Nat. Mater.* **15** 154–8
[45] Pisoni A, Gaál R, Zeugner A, Falkowski V, Isaeva A, Huppertz H, Autès G, Yazyev O and Forró L 2017 Pressure effect and superconductivity in the β-Bi_4I_4 topological insulator *Phys. Rev.* B **95** 235149
[46] Qi Y *et al* 2018 Pressure-induced superconductivity and topological quantum phase transitions in a quasi-one-dimensional topological insulator: Bi_4I_4 *npj Quantum Mater.* **3** 4
[47] Liu C-C, Zhou J-J, Yao Y and Zhang F 2016 Weak topological insulators and composite Weyl semimetals: β-Bi_4X_4 (X = Br,I) *Phys. Rev. Lett.* **116** 66801
[48] Zhou J-J, Feng W, Liu C-C, Guan S and Yao Y 2014 Large-gap quantum spin hall insulator in single layer bismuth monobromide Bi_4Br_4 *Nano Lett.* **14** 4767–71
[49] Kresse G and Furthmüller J 1996 Efficient iterative schemes for *ab initio* total-energy calculations using a plane-wave basis set *Phys. Rev.* B **54** 11169–86
[50] Souza I, Marzari N and Vanderbilt D 2001 Maximally localized wannier functions for entangled energy bands *Phys. Rev.* B **65** 035109
[51] Li G, Luican A, Dos Santos J L, Neto A C, Reina A, Kong J and Andrei E 2010 Observation of van Hove singularities in twisted graphene layersan hove singularities in twisted graphene layers *Nat. Phys.* **6** 109–13
[52] Nilsson J, Neto A C, Peres N and Guinea F 2006 Electron–electron interactions and the phase diagram of a graphene bilayer *Phys. Rev.* B **73** 214418
[53] Nandkishore R, Levitov L and Chubukov A 2012 Chiral superconductivity from repulsive interactions in doped graphene *Nat. Phys.* **8** 158–63
[54] Edelstein V M 1990 Spin polarization of conduction electrons induced by electric current in two-dimensional asymmetric electron systems *Solid State Commun.* **73** 233–5
[55] Li H *et al* 2015 Intraband and interband spin–orbit torques in noncentrosymmetric ferromagnets *Phys. Rev.* B **91** 134402
[56] Kato Y K, Myers R C, Gossard A C and Awschalom D D 2004 Observation of the spin Hall *Science* **306** 1910–3
[57] Perdew J P, Burke K and Ernzerhof M 1996 Generalized gradient approximation made simple *Phys. Rev. Lett.* **77** 3865–8
[58] Blöchl P E 1994 Projector augmented-wave method *Phys. Rev.* B **50** 17953–79
[59] Kresse G and Joubert D 1999 From ultrasoft pseudopotentials to the projector augmented-wave method *Phys. Rev.* B **59** 1758–75
[60] Kresse G and Hafner J 1993 *Ab initio* molecular dynamics for open-shell transition metals *Phys. Rev.* B **48** 13115–8
[61] Kresse G and Furthmüller J 1996 Efficiency of *ab initio* total energy calculations for metals and semiconductors using a plane-wave basis set *Comput. Mater. Sci.* **6** 15–50
[62] Franchini C, Kováčik R, Marsman M, Sathyanarayana Murthy S, He J, Ederer C and Kresse G 2012 Maximally localized Wannier functions in LaMnO 3 within PBE + U, hybrid functionals and partially self-consistent GW: an efficient route to construct *ab initio* tight-binding parameters for e.g. perovskites *J. Phys.: Condens. Matter* **24** 235602
[63] Bryant G W 1985 Surface states of ternary semiconductor alloys: effect of alloy fluctuations in one-dimensional models with realistic atoms *Phys. Rev.* B **31** 5166–77